ELSEVIER

The multi-angle view of MISR detects oil slicks under sun glitter conditions

Guillem Chust *, Yolanda Sagarminaga

AZTI-Tecnalia, Marine Research Division, Herrera kaia portualdea z/g, 20110 Pasaia, Spain

Abstract

We tested the use of the Multi-angle Imaging SpectroRadiometer (MISR) for detecting oil spills in the Lake Maracaibo, Venezuela, that were caused by a series of accidents between December 2002 and March 2003. The MISR sensor, onboard the Terra satellite, utilises nine cameras pointed at fixed angles, ranging from nadir to $\pm 70.5°$. Based upon the Bidirectional Reflectance Factor, a contrast function and a classification accuracy assessment, it is shown, for two images examined under sun glint conditions, that the MISR sensor provides a better capability for oil spill discrimination, than the single-view MODIS-250 m data. Analysis of the multi-angle MISR red band indicates that oil spills appear with greater contrast in those view angles affected by sun glitter as a result of local changes in surface roughness caused by the hydrocarbons. Although limited by cloud cover, the capability of the MISR instrument for oil spill discrimination, together with its weekly temporal resolution and open data access, have the potential for improving the operational monitoring of oil releases.
© 2006 Elsevier Inc. All rights reserved.

1. Introduction

The anthropogenic release of oil into the oceans from tankers, ships and pipelines may have significant ecological and socioeconomic impacts on coastal environments. A substantial part of oil pollution originates from operative discharges from ships (European Space Agency, 2002; Pavlakis et al., 1996). Early detection of accidental or deliberate oil spills can prevent serious damages on littoral habitats and assist in the identification of polluters. At present, there exist multiple instruments capable of detecting oil spills (Bedborough, 1996; Brekke & Solberg, 2005; Fingas & Brown, 2000; Fingas & Brown, 1997; MacDonald et al., 1993), using both space and airborne platforms: radar (SAR, SLAR), UV, microwave radiometers, photographic cameras, video cameras, electro-optical sensors within the visible and infrared, and laser fluorosensors. As the studies of Fingas and Brown (2000) and Brekke and Solberg (2005) conclude, each instrument has strengths and deficiencies, so there is no single instrument that is best at detecting spills but rather multiple sensors are needed to provide the best discrimination. Active sensors such as Synthetic Aperture

Radar (SAR), have been used commonly for ocean pollution detection (e.g. DiGiacomo et al., 2004; Gade & Alpers, 1999); they are preferred to optical sensors due to their all-weather and all-day capabilities (Brekke & Solberg, 2005). However, SAR data have also several disadvantages: 1) there is generally no daily sampling on a routine basis, 2) their application to oil spill detection is limited to a small range of wind speed (1.5–6 m/s, Liu et al., 2000; at high wind speeds, >10 m/s, few oil spills can be detected in the SAR images, Gade et al., 2000); likewise, the wind conditions can also limit the use of optical sensors since high winds mix the oil into the surface waters, thus removing its presence as a surface slick; 3) features such as phytoplankton and freshwater slicks may have similar appearance as oil slicks on SAR, which results in ambiguous detection of the oil itself (Lin et al., 2002), and 4) the images may be expensive to purchase. Although optical sensors are affected by cloud cover, they have the advantage of permitting the discrimination between algal blooms and oil spills, based on multispectral information (Brekke & Solberg, 2005). For instance, the Visible and Near Infrared (VNIR) bands of MODIS have been shown to be effective in detecting oil slicks in Lake Maracaibo, Venezuela (Hu et al., 2003), although oil reflects particularly well in the thermal infrared portion of the spectrum (Salisbury et al., 1993).

---

* Corresponding author. Tel.: +34 943004800; fax: +34 943004801.
  E-mail address: gchust@pas.azti.es (G. Chust).

Remotely sensed land surface reflectance has been shown to depend upon changing sun and sensor viewing geometry. This dependence, termed the Bidirectional Reflectance Distribution Function (BRDF), is highly anisotropic for volumetric targets such as atmospheric aerosols and vegetation. Oceanographic features can also manifest anisotropy, and this phenomenon can be highlighted under sun glitter conditions. Sun glitter involves the direct reflection of sunlight from the water surface. The presence of glitter in an image has been considered often to represent a serious data loss. Conversely, the acquisition of imagery containing areas dominated by sun glitter can, in certain circumstances, be of considerable value (Khattak et al., 1991; MacDonald et al., 1993). This is the case of surface wind speed (Cox & Munk, 1954), oceanic internal waves (Matthews, 2005), shallow water bottom topography (Hennings et al., 1994) and river plume frontal boundaries (Matthews et al., 1997). Furthermore, water surfaces affected by sun glitter often manifest brightness reversal between two different views, in which relatively bright features at one angle appear dark in the other view. Such a region of brightness reversal can be indicative of a locally rough or smooth surface texture (Matthews, 2005), this may be found, for example, in the surroundings of internal waves or ship wakes. The optical response of the state of the sea surface roughness can be described by either the BRDF, or by the contrast distribution function (Otremba & Piskozub, 2001). The need for multi-view observations has led to the incorporation of such measurements in several spaceborne missions (Asner et al., 1998) such as the Advanced Spaceborne Thermal Emission and Reflection Radiometer (ASTER), Multi-angle Imaging SpectroRadiometer (MISR), POLarization and Directonality of the Earth's Reflectance (POLDER), and the Advanced Land Observing Satellite (ALOS).

In this contribution, the use of the Multi-angle Imaging SpectroRadiometer (MISR) is compared to the MODIS bands, at 250 m, for detecting oil spills in Lake Maracaibo, a coastal lagoon connected to the Gulf of Venezuela. Between December 2002 and March 2003, oil companies operating in the Lake Maracaibo suffered a series of accidents, which led to extensive oil spills. The detection of oil marine pollutants by the MISR has not been investigated extensively; this is despite a short Note which appeared on this particular issue by the Jet Propulsion Laboratory (NASA, http://www-misr.jpl.nasa.gov/gallery/galhistory/2003_may_21.html). This omission is not surprising, since the multi-angle view of MISR was designed mainly for distinguishing different types of atmospheric particles (aerosols), cloud geometry, land surface covers, and for use in the construction of 3-D models (Diner et al., 1998). Specifically, the questions addressed here are: which MISR view angles are the most appropriate to detect oil-contaminated waters? and at which sunlight conditions? Likewise, can the multi-angle measurements enhance the oil discrimination in relation to a single-angle optical imager?

2. MISR and MODIS imagery of oil slicks

The MISR sensor consists of nine pushbroom cameras, one viewing the nadir (vertically downward) direction (designated

An) and four each viewing the forward and backward directions along the spacecraft ground track, labelled Df, Cf, Bf, Af, and Aa, Ba, Ca, Da, respectively. The corresponding viewing zenith angles are: 70.5° (Df, Da), 60° (Cf, Ca), 45.6° (Bf, Ba), 26.1° (Af, Aa) and 0° (An). The overall time delay, between the Df and Da cameras, is 7 min. It observes the Earth in four visible and near infrared (NIR) spectral bands (446, 558, 672, and 866 nm), with a cross-track ground spatial resolution of 275 m–1.1 km. Only images sampled at medium-resolution (275 m) were used in this study, i.e. the red band (672 nm) at all nine view angles, and the four spectral bands at nadir view. The MISR swath width is 380 km (cross-track). The operational data products from MISR are described in Bull et al. (2005).

The medium-resolution MISR radiance imagery (Level 1B2), from 1 December 2002 to 9 March 2003, has been examined for Lake Maracaibo (Fig. 1). The location of spills in MISR images was extracted from the studies undertaken by the Jet Propulsion Laboratory (NASA), with MISR (http://www-misr.jpl.nasa.gov/gallery/galhistory/2003_may_21.html); likewise, by Hu et al. (2003) who had identified already oil spills in the Lake with MODIS-250 m data, acquired on the same dates, and used airborne photography for ground truth. The spills dispersed in the Lake as an oil film floating on the surface. Of the 19 image sets available for this period (obtained from the NASA Langley Research Center Atmospheric Sciences Data Center), images were selected that were free of clouds. Amongst these images, the most apparent oil spill patches were visually identified in those collected during December 2002 and January 2003 (26/12/02, 4/01/03, 20/01/03 and 27/01/03), using the 275-m resolution red band. Finally, multiple angle analysis was performed on the image sets acquired on 26 December 2002 and 20 January 2003 (Fig. 1), which presented several oil spills and optimal cloud cover conditions.

The corresponding MODIS images acquired on these two dates have been analysed also, for comparative purposes. The MODIS sensor aboard the Earth Observing System (EOS) satellites Terra and Aqua, provides a morning and afternoon view with global, near-daily repeat coverage. Such data are distributed by the Land Processes Distributed Active Archive Center (U.S. Geological Survey Center for Earth Resources Observation and Science). The Level 1B calibrated-radiances of MODIS band 1 (645 nm, red) and band 2 (856 nm, near infrared) were used. These bands have a spatial resolution of 250 m. The MODIS swath width is 2330 km.

The observational geometry parameters of the two selected dates involved in sun glitter conditions were contained in the corresponding products (the general conditions are described in Hennings et al., 1994, and in Matthews, 2005). The geometric parameters are defined as follows (see also Bull et al., 2005). Solar zenith is the angle between the $+z$ axis (which points into the earth, in the direction opposite the ellipsoid normal) and a vector anchored at the ground point extending into the earth in the direction of photon travel from the sun. Solar azimuth is the angle measured clockwise from the local north vector to the projection onto the x,y plane of the photon travel direction vector. This "photon travel azimuth" convention differs from the familiar "look azimuth" by 180°. Camera zenith is the angle
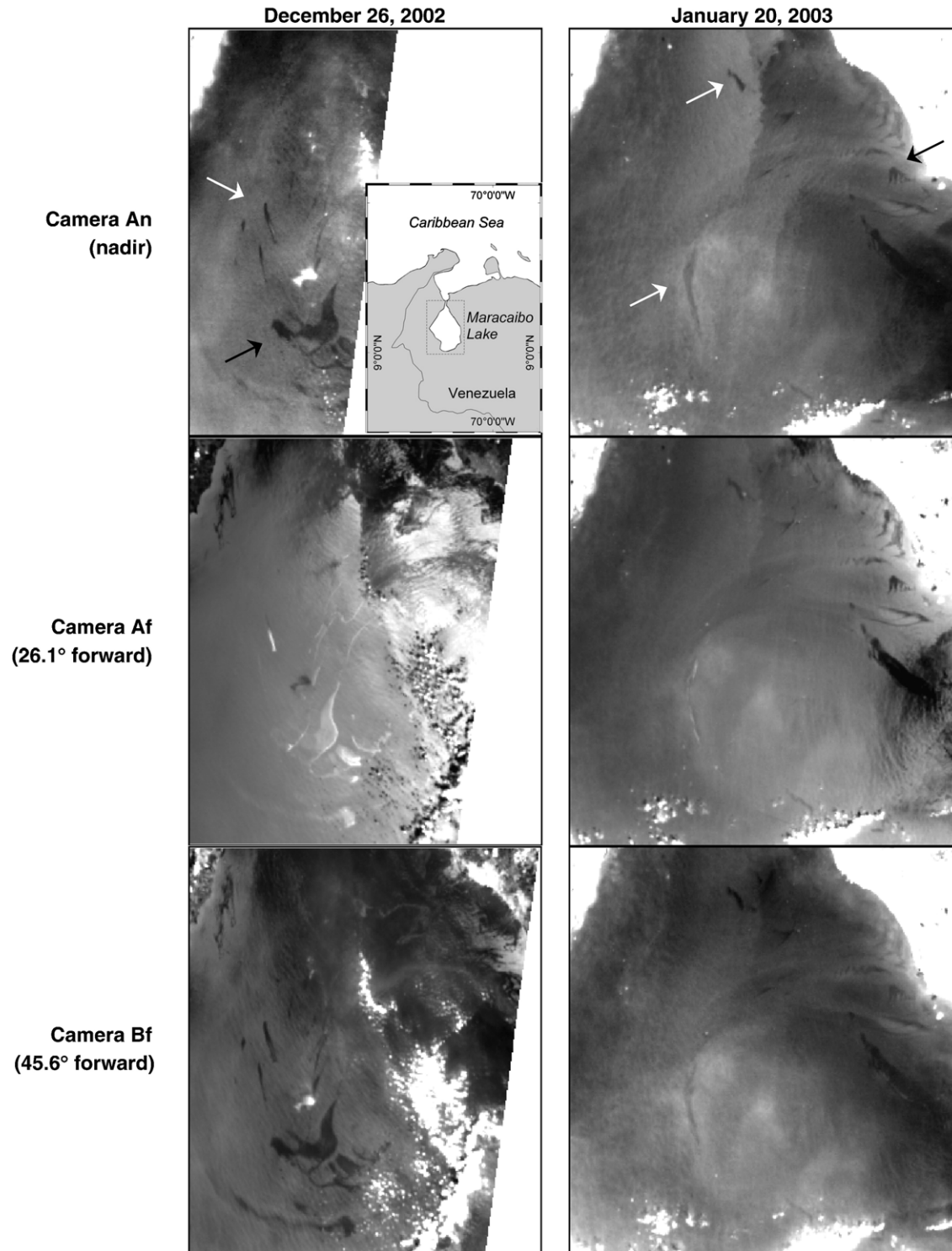
Fig. 1. Series of MISR (672 nm) images of a portion of the Lake Maracaibo taken by cameras viewing 0° (camera An), 26.1° forward (Af), and 45.6° forward (Bf). Black arrows on the An camera image indicate the oil spills used in the BRF analysis in the present paper; the white arrows indicate other main slicks used in the validation of supervised classifications. The inset image shows the location of Lake Maracaibo within the coastal region of the Gulf of Venezuela.

between the $-z$ axis and the "camera vector", which is anchored at the ground point and is directed toward the camera in the direction of photon travel. Camera azimuth is the angle measured clockwise from the local north vector to the projection onto the x,y plane of the camera vector. For the images analysed, solar zenith (ζ) and azimuth (Φ) angles were: $\zeta = 38.2°$, $\Phi = 330.9°$ (26/12/ 2002), and $\zeta = 36.8°$, $\Phi = 324.5°$ (20/01/03). For Af view, the camera azimuth angles were 340.3° and 16.2° on 26/12/02 and 20/01/03, respectively; the camera zenith angles were: 30.1° and 28.5° on 26/12/02 and 20/01/03, respectively.

Near-surface wind speeds were low to moderate: 4.4 m/s (26/12/2002) and 5.6 m/s (20/01/03); as measured by QuikSCAT

(Level 3 Daily, 0.25 × 0.25° Gridded Ocean Wind Vectors, JPL SeaWinds Project). These wind values fall within the range at which hydrocarbons dampen sea waves.

3. Bidirectional reflectance factor and discrimination of oil slicks

Radiance values were converted initially to the top-of-atmosphere bidirectional reflectance factor (BRF), for each band and view angle. The Bidirectional Reflectance Factor (BRF) is defined as the observed radiance divided by the radiance from a perfect Lambertian reflector, under conditions in which the illumination is from a single direction (Martonchik et al., 1998). We used the following equation to calculate the top-of-atmosphere BRF (see Bull et al., 2005):

$$\mathrm{BRF}(-\mu, \mu_0, \Phi - \Phi_0) = \frac{\pi L(-\mu, \mu_0, \Phi - \Phi_0) \cdot D^2}{\mu_0 E_{0,b}^{\mathrm{std}}},$$

where L is the measured radiance from MISR Level 1B2 radiance product, μ is the cosine of viewing zenith angle, μ_0 is the cosine of solar zenith angle, $\Phi - \Phi_0$ is the difference between solar and viewing azimuth angles, D is the approximate distance, in astronomical units, between the centre of the Earth and the centre of the Sun, at the time that the MISR observes the first pixel in the swath, and $E_{0,b}^{\mathrm{std}}$ (W m^{-2} μm^{-1}) is the standardised band-weighted solar irradiance.

The BRF sampled within the oil slick patches and their surroundings (oil-free water) were analysed at different view angles (i.e. 9 cameras) within the red band, and they have been compared with glitter conditions and glitter angle. The BRF samples were extracted by selecting visually all pixels within the oil slick patches, excluding boundary pixels, and unpolluted areas adjacent to each slick; one slick was chosen for each date (indicated in black arrows in Fig. 1). The glitter conditions and glitter angle were contained in the corresponding products described in Bull et al. (2005), obtained also from the Langley Atmospheric Data Center. Glitter conditions are represented by a binary mask image, providing a glitter contaminated/non-contaminated pixel information at 1.1 × 1.1 km. Glitter angle (°) is the angle between a vector from the observed point to the camera and a vector pointing in the specular reflection direction; it is provided at 17.6 × 17.6 km spatial resolution.

The potential discrimination of oil pollutants, using MISR and MODIS-250m, has been assessed by 1) a comparison of radiance means between oil slick patches and their surroundings (using a contrast function and the Wilks' Lambda test) for each spectral band at nadir, and for each view angle; and 2) supervised classifications and the associated accuracy assessment. The contrast function (Otremba & Piskozub, 2001), at a given wavelength λ, is expressed by the following relationship:

$$c(\zeta_r, \Phi_r, \lambda) = \frac{L_p(\zeta_r, \Phi_r, \lambda) - L_c(\zeta_r, \Phi_r, \lambda)}{L_c(\zeta_c, \Phi_r, \lambda)}$$

where L_p (ζ_r, Φ_r, λ) is the upward radiance above the polluted sea surface in a direction defined by a zenith angle ζ_r and an azimuth angle Φ_r, and L_c (ζ_r, Φ_r, λ) is the upward radiance

above the clean sea surface. The Wilks' Lambda is based on a discriminant analysis and tests the hypothesis that the means are equal across classes (i.e. polluted vs clean waters). Wilks' Lambda close to 0 indicates that the classes are different. A per-pixel supervised classification method based on maximum likelihood algorithm was used to assess the discrimination between the oil slicks and two types of oil-free water. These two types of unpolluted waters have been defined to cover the maximal range in radiances on the water state of the Lake, at red wavelengths; thus, Type 1 refers to relatively high radiance values and Type 2 refers to relatively low radiances. Two independent training sites have been created; one to calculate the statistics needed for the classification; the other to evaluate the reliability of classifications. Several slicks for each date were used for classification (indicated in black and white arrows in Fig. 1). Prior to performing the classification process, the Jeffries–Matusita separability index (Thomas et al., 1987) was calculated between pairs of classes using the first training site set. As measures of classification accuracy, the producer's accuracy (PA) and the user's accuracy (UA) for each class, were used (Stehman, 1997). These accuracy measurements are derived from the confusion matrix which is created from the comparison between the classification and the verification data (a set of training sites independent of that used for the classification process). Several classifications were performed combining those MISR bands and cameras with higher discrimination potential, based on the Wilks' Lambda test; likewise, one classification with MODIS (using NIR and red bands).

4. Results and discussion

Fig. 1 shows a portion of the images at different view angles acquired by the 275-m resolution MISR red band (672 nm) of a part of Lake Maracaibo on 26 December 2002 and 20 January 2003. On these two dates, oil slicks were identified mainly in the three views affected mostly by sun glitter (Fig. 2c,d): nadir, 26° and 46° forward, i.e. An, Af and Bf cameras, respectively. At nadir and 46° forward, all the oil slicks appear as darker zones on the image. At 26° forward, which is the view closest to the specular reflection on the two dates (Fig. 2c,d), the oil slick appears brighter on 26 December 2002. On 20 January 2003, where the glitter angle (29.8°) is not as close to the specular angle as on 26 December 2002 (10.9°), the slicks to the north and east appear darker, whilst the central slick is less visible. As previously shown, the differences in sun glitter conditions between the two dates depend mainly upon the different solar azimuth angle ($\Delta = 6.4°$) and Af camera azimuth angle ($\Delta = 35.8°$).

Two large oil slicks, one for each date (indicated with black arrows in Fig. 1), have been selected subsequently for analysis, to extract BRF values, contrast function and Wilks' Lambda. For December 2002, Fig. 2a shows that the differences in the BRF values are greater for the Af and Bf cameras, in which calm water regions are expected to be affected maximally by sun glitter (Fig. 2c). At the An view, the oil has also an important contrast value (Table 1). The Wilks' Lambda provides slightly different results; it indicates that Bf is the camera within
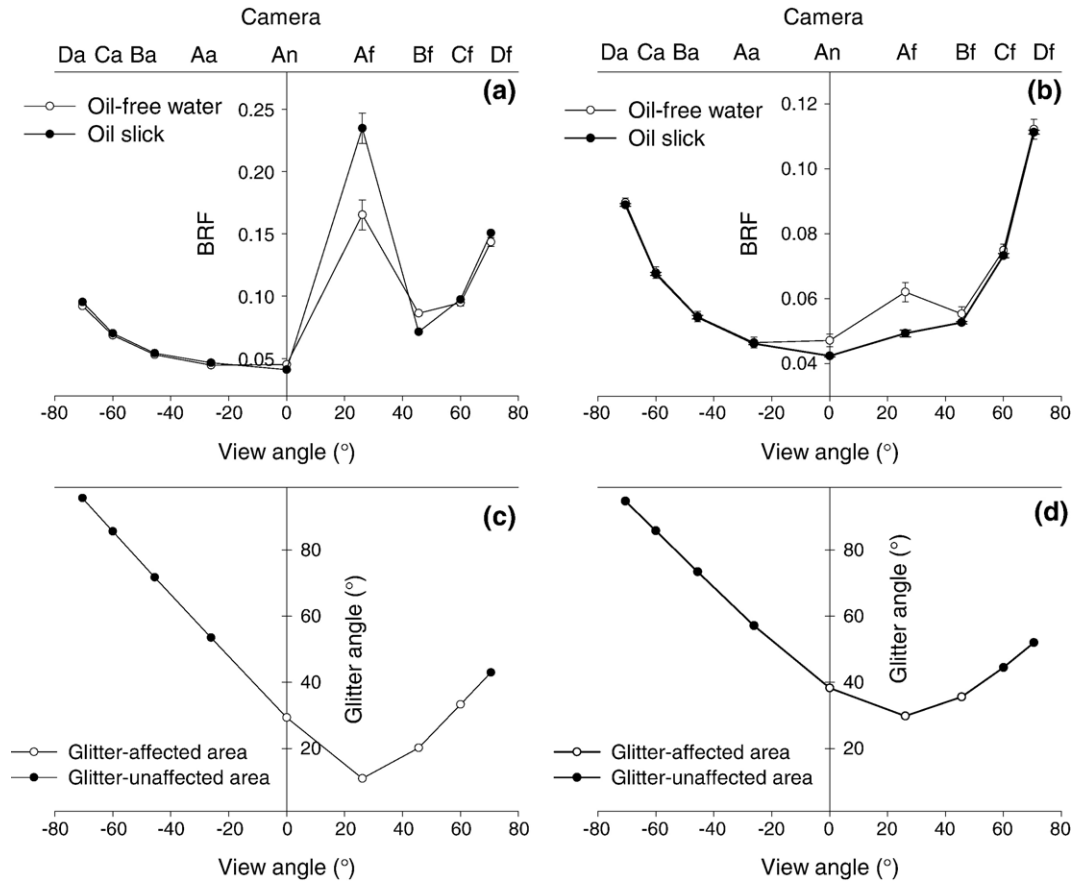
Fig. 2. The top-of-atmosphere BRF values from the MISR (672 nm) image within the oil slicks on the Lake present on (a) 26 December 2002 and (b) 20 January 2003, compared with the surrounding clean water at different view angles. Error bars represent ± standard deviation. For December 2002, the oil and unpolluted patches contained 307 and 206 pixels, respectively; for January 2003, the oil and unpolluted patches contained 15 and 243 pixels, respectively. The glitter angle and glitter condition of the area affected by spills at the corresponding dates: (c) 26 December 2002; and (d) 20 January 2003.

the red band that better discriminates polluted waters, followed by An; whilst Af, the closest to the specular reflection, is not as capable as An and Bf. Although the Wilks' Lambda test indicates that slicks can be discriminated statistically on all of the cameras, those which are far from the specular reflection have less discrimination potential. For January 2003, the oil slick shows maximal BRF differences in the Af and An cameras, followed by Bf (Fig. 2b); this is in accordance to the sun glitter conditions (Fig. 2d), high contrast and low Wilks' Lambda values (Table 1). For the two dates, both the contrast and the Wilks' Lambda indicates that NIR is the most appropriate, amongst the four VNIR spectral bands at nadir, to discriminate oil slicks, this is followed by the red band in most of the cases (Table 1). The red and the NIR bands of MODIS have similar values of contrast and Wilks' Lambda compared to the corresponding bands of MISR's An camera (Table 1).

These results indicate that the direct reflection of sunlight arrives from the oil-contaminated water at 26° view on 26 December 2002. The oil-contaminated waters in that date manifest brightness reversal between the moderately near specular angles (nadir and 46° forward-looking view) and the very-near specular angle (26° view). Such regions of brightness reversal can be indicators of local roughness changes in surface texture (Matthews, 2005); and, as is well known, oil slicks tend to

dampen surface capillary waves, making the water smoother than the surrounding oil-free water. As a general rule, the optical contrast of an oil film on a sea surface, at specific wind conditions and at red wavelengths, depends on three domains of the glitter angle: 1) at angles (>40°) not affected by sun glitter, slicks are practically not detected; 2) at angles (<15°) very near to the specular angle, the slicks appear brighter than the unpolluted areas; and 3) at angles (15°–40°) moderately near to the specular angle, the slicks appear darker, since oil is more absorbing than the surrounding water. This is the case for December 2002, whilst for January 2003 a brightness reversal is not present, because of higher sun glitter angles (>15°). The threshold values of glitter angles indicated here are obtained from the two images; in order to estimate these thresholds with confidence, more images are needed.

Since An, Af, and Bf were identified as the cameras with high discrimination potential, four classifications were performed, combining these cameras with spectral bands at nadir: 1) An view (NIR and red bands); 2) An (NIR and red), Af and Bf; 3) An (4 bands), Af and Bf; and 4) An (NIR and red), and all cameras excluding Af. By comparing the first two classifications, the contribution of multi-angle with respect to just the An view is tested. The third classification tests the joint contribution of spectral bands with multi-angle view. By excluding Af, the fourth

Table 1

Contrast values and Wilks' Lambda test in oil slicks in relation to the surroundings waters, on 26 December 2002 and 20 January 2003, for 275-m spatial resolution MISR and MODIS-250 m

Sensor	Band	Camera	December 26, 2002		January 20, 2003	
			Contrast	Wilks' Lambda	Contrast	Wilks' Lambda
MISR	Blue	An	−0.017	0.135**	−0.023	0.755**
	Green	An	−0.052	0.073**	−0.043	0.937**
	NIR	An	−0.165	0.044**	−0.178	0.571**
	Red	Df	0.050	0.360**	−0.008	0.995
	Red	Cf	0.027	0.240**	−0.022	0.958**
	Red	Bf	−0.172	0.046**	−0.049	0.919**
	Red	Af	0.420	0.238**	−0.205	0.504**
	Red	An	−0.092	0.056**	−0.102	0.761**
	Red	Aa	0.042	0.408**	−0.007	0.998
	Red	Ba	0.022	0.412**	−0.003	0.999
	Red	Ca	0.023	0.569**	−0.005	0.997
	Red	Da	0.033	0.691**	−0.008	0.985*
MODIS-250 m	Red	–	−0.093	0.095**	−0.099	0.690**
	NIR	–	−0.193	0.091**	−0.217	0.464**

* $0.001 < p < 0.05$; where p is the p-value associated to the Wilks' Lambda test.
** $p \leq 0.001$.

classification tests the effect of removing brightness reversal in the image set of 2003. The Jeffries–Matusita index indicates high separability between oil and clean water Type 1 in all cases at the two dates, including MODIS (Table 2). Conversely, low values of separability index were found between the oil and clean water Type 2, in two of the cases: using An (red and NIR) for MISR, and red and NIR for MODIS. The classification accuracy assessment (Table 2) has revealed that the two classifications combining Af and Bf cameras with spectral bands in An produced high values of producer's (PA) or user's accuracy (UA) (higher than 81% for December 2002 and higher than 70% for January 2003). The classification using only the red and NIR bands in An produced low accuracy values (PA or UA inferior to 50%). These latter values are similar to the corresponding classification of the MODIS bands. The classification using all cameras excluding Af produced higher accuracy values for the December 2002 (PA=65% and UA=75%) than that of MODIS (PA=53% and UA=30%). This observation indicates that the varying appearance of spills as a function of view angles alone (without the presence of brightness reversal) can improve oil discrimination in comparison to a single-view optical imager. However, the presence of brightness reversal, in particular,

enhances this discrimination potential. In the case of January 2003, the classification using all cameras excluding Af produced a low producer's accuracy value (46%); once again, this indicates the importance of the Af camera in oil discrimination. The general low accuracy determinations in January 2003, compared with December 2002, is due to the absence of brightness reversal; likewise, to the size of the oil patches. In January 2003, the oil patch was small and thin and, hence, the radiance value is affected by the neighbouring pixels.

5. Conclusions and perspectives

The findings of the present study show, at least for the two images examined here, that the 275 m resolution MISR sensor provides a capability for oil spill discrimination in coastal environments which is better than MODIS-250 m sensor under sun glint. The results of the MISR red band, at different angle views, indicate that oil spills appear in more contrast in those views affected by sun glitter. The changes in the radiance-related quantities, as a function of view angle, depend on the composition, density, and geometric structure of the reflecting surface (i.e. water state); they are exemplified by glitters, shadows, and volumetric scattering (Diner et al., 2005). The results obtained here enable the conclusions to be reached that, spectrally, oil slicks can be detected within the red band; this contrast is highlighted under glitter conditions, as a result of local changes in surface roughness caused by the presence of hydrocarbons. Dampening of water surface waves by oil slicks occurs at low to moderate winds, which were the prevailing conditions on the two dates discussed here. For the two sets of images examined, three domains of oil radiometric response as a function of view angle have been identified: 1) at angles unaffected by sun glitter, slicks were not identified or appeared slightly darker than adjacent unpolluted areas; 2) at angles affected by sun glitter, but moderately near to the specular direction, slicks appeared darker because they are more absorbent than unpolluted waters; and 3) at the specular angle, or very near to, the slicks appeared brighter. The specific range of sun glitter angles which dictates the radiometric contrast depend on wind speed conditions (Otremba & Piskozub, 2001). This phenomenon is well established in SAR imagery, where the presence of hydrocarbon smoothes water surface roughness and causes a reduction in the backscattering. The detection of oceanic surface films by MISR depends on the factors

Table 2

Jeffries–Matusita separability index and classification accuracies of oil slicks *vs* clean waters combining different bands and cameras of MISR and MODIS-250 m (spills of 26 December 2002 and of 20 January 2003). Key, PA: Producer's accuracy; UA: User's accuracy; Clean 1: oil-free water type 1; and Clean 2: oil-free water type 2 (see text for explanation)

Sensor	Bands and cameras	December 26, 2002				January 20, 2003			
		Jeffries–Matusita		PA	UA	Jeffries–Matusita		PA	UA
		Oil *vs* Clean 1	Oil *vs* Clean 2	Oil	Oil	Oil *vs* Clean 1	Oil *vs* Clean 2	Oil	Oil
MISR	An (NIR, red)	1.99	0.54	49.71	21.88	1.87	0.53	47.58	29.49
	An (NIR, red), Af, Bf	2.00	1.96	98.37	93.30	1.99	1.48	70.63	100.0
	An (NIR, red, green, blue), Af, Bf	2.00	2.00	81.58	100.0	1.99	1.91	73.61	94.29
	An (NIR, red), all cameras excluding Af	1.99	1.96	65.20	75.34	1.97	1.99	45.72	82.55
MODIS	NIR, red	1.99	0.79	53.44	29.53	1.88	0.56	77.17	48.76

modulating surface roughness, such as wind speeds as it does for SAR instruments. The multi-angular vision of the MISR sensor establishes a basis for the understanding of the visual interpretation of water features at particular sunlight conditions. Within an application perspective, the varying appearance of spills as a function of view angles under sun glitter enhances the reliability of automatic oil detection using standard image classification methods as shown here, this is especially true when brightness reversal is present. Whilst sun glitter may occur frequently in several of the MISR cameras, specific conditions to acquire images very near to the specular angle constrains the appearance of the brightness reversal.

On the basis that the MISR instrument was designed originally for atmospheric and land applications, it is not configured ideally for the observation of coastal water bodies. Similar limitations are shared, for example, by the two-view near-infrared band of the ASTER sensor. The recently-launched satellite ALOS (Igarashi, 2001), which carries the Panchromatic Remote-sensing Instrument for Stereo Mapping (PRISM) and the Advanced Visible and Near Infrared Radiometer type 2 (AVNIR-2), may return data of great value for the observation of coastal waters. An improved stereo imaging device dedicated to coast observation at suitable scales, would require at least: 1) VNIR wavelength bands acquired at medium spatial resolution, or higher, so that the sensor could return estimates of water bio-physical parameters and oil slicks under sun glitter conditions; and 2) a swath width sufficient to provide near-daily repeated coverage, in particular for routine oil detection. A research issue that must be addressed with MISR is the evaluation of different types, thickness and heaviness of hydrocarbons. The possibility to test the radiometric response of water features as a function of the view angle and spectral information with MISR data, may help researchers in the interpretation of oceanographic features and in designing new instrumentation for use in space.

The capabilities of multi-angle MISR data to provide medium-resolution, weekly images and to detect oil pollutants, together with its free cost, have the potential to improve operational systems of oil release monitoring in coastal systems. In this context, the MODIS-250 m sensor is also of great value for complementing MISR images because it provides daily images. Since oil pollution control agencies should respond rapidly to a relatively rare event, they need to be cost effective coordinating satellite overpasses and aerial surveillance flights. The coordinated use of satellite imagery and aerial surveillance flights is presently operational in many countries in Northern Europe (Brekke & Solberg, 2005). Within the spaceborne-based strategy for routine, wide surveillance of marine water quality, the capabilities of optical multi-angle imaging, such as from MISR, will improve and complement the other sensors including radar being used for ocean pollution surveillance.

Acknowledgements

References

Asner, G. P., Braswell, B. H., Schimel, D. S., & Wessman, C. A. (1998). Ecological research needs from multiangle remote sensing data. *Remote Sensing of Environment*, *63*, 155−165.

Bedborough, D. R. (1996). The use of satellites to detect oil slicks at sea. *Spill Science and Technology Bulletin*, *3*, 3−10.

Brekke, C., & Solberg, A. H. S. (2005). Oil spill detection by satellite remote sensing. *Remote Sensing of Environment*, *95*, 1−13.

Bull, M., Matthews, J., Moroney, C., & Smyth, M. (2005). *MISR data products specifications*. Jet Propulsion Laboratory. http://eosweb.larc.nasa.gov/PRODOCS/misr/DPS/DPS_v40_RevN.pdf

Cox, C., & Munk, W. H. (1954). The measurement of the roughness of the sea surface from photographs of the sun's glitter. *Journal of the Optical Society of America*, *44*, 838−850.

DiGiacomo, P. M., Washburn, L., Holt, B., & Jones, B. H. (2004). Coastal pollution hazards in southern California observed by SAR imagery: Stormwater plumes, wastewater plumes, and natural hydrocarbon seeps. *Marine Pollution Bulletin*, *49*, 1013−1024.

Diner, D. J., Beckert, J. C., Reilly, T. H., Bruegge, C. J., Conel, J. E., Kahn, R., et al. (1998). Multi-angle Imaging SpectroRadiometer (MISR) description and experiment overview. *IEEE Transactions on Geoscience and Remote Sensing*, *36*, 1072−1087.

Diner, D. J., Braswell, B. H, Davies, R., Gobron, N., Hu, J. N., Jin, Y. F., et al. (2005). The value of multiangle measurements for retrieving structurally and radiatively consistent properties of clouds, aerosols, and surfaces. *Remote Sensing of Environment*, *97*, 495−518.

European Space Agency (2002), *ASAR product handbook*. Tech. rep., European Space Agancy-ENVISAT Product Handbook, Issue 1.1, 1 December 2002.

Fingas, M., & Brown, C. (2000). Oil-spill remote sensing — An update. *Sea Technology*, *41*, 21−26.

Fingas, M. F., & Brown, C. E. (1997). Review of oil spill remote sensing. *Spill Science and Technology Bulletin*, *4*, 199−208.

Gade, M., & Alpers, W. (1999). Using ERS-2 SAR images for routine observation of marine pollution in European coastal waters. *The Science of the Total Environment*, *237/238*, 441−448.

Gade, M., Scholz, J., & von Viebahn, C. (2000). On the detectability of marine oil pollution in European marginal waters by means of ERS SAR imagery. *Proceedings of the IGARSS*, *6*, 2510−2512.

Hu, C., Muller-Karger, F., Taylor, C. J., Myhre, D., Murch, B., Odriozola, A. L., et al. (2003). MODIS detects oil spills in Lake Maracaibo, Venezuela. *Eos, Transactions of the American Geophysical Union*, *84*, 313−319.

Hennings, I., Matthews, J. P., & Metzner, M. (1994). Sun glitter radiance and radar cross-section modulations of the sea bed. *Journal of Geophysical Research*, *99*, 16303−16326.

Igarashi, T. (2001). ALOS mission requirement and sensor specifications. *Advances in Space Research*, *28*, 127−131.

Khattak, S., Vaughan, R. A., & Cracknell, A. P. (1991). Sunglint and its observation in AVHRR data. *Remote Sensing of Environment*, *37*, 101−116.

Lin, I. I., Wen, L. S., Liu, K. K., & Tsai, W. T. (2002). Evidence and quantification of the correlation between radar backscatter and ocean colour supported by simultaneously acquired in situ sea truth. *Geophysical Research Letters*, *29*, 1−4.

Liu, A. K. S., Wu, Y., Tseng, W. Y., & Pichel, W. G. (2000). Wavelet analysis of SAR images for coastal monitoring. *Canadian Journal of Remote Sensing*, *26*, 494−500.

MacDonald, I. R., Guinasso, N. L., Jr., Ackleson, S. G., Amos, J. F., Duckworth, R., Sassen, R., et al. (1993). Natural oil slicks in the Gulf of Mexico visible from space. *Journal of Geophysical Research − Oceans*, *C9*(98), 16351−16364.

Martonchik, J. V., Diner, D. J., Pinty, B., Verstraete, M. M., Myneni, R. B., Knayazikhin, Y., et al. (1998). Determination of land and ocean reflective, radiative, and biophysical properties using multiangle imaging. *IEEE Transactions on Geoscience and Remote Sensing*, *36*, 1266−1281.

Matthews, J. (2005). Stereo observation of lakes and coastal zones using ASTER imagery. *Remote Sensing of Environment, 99,* 16−30.

Matthews, J. P., Wismann, V., Lwiza, K., Romeiser, R., Hennings, I., & de Loor, G. P. (1997). The observation of the surface roughness characteristics of the Rhine plume frontal boundaries by simultaneous Airborne Thematic Mapper and multifrequency helicopter-borne radar scatterometer. *International Journal of Remote Sensing, 18,* 2021−2033.

Otremba, Z., & Piskozub, J. (2001). Modelling of the optical contrast of an oil film on a sea surface. *Optics Express, 9,* 411−416.

Pavlakis, P., Sieber, A., & Alexandry, S. (1996). Monitoring oil-spill pollution in the Mediterranean with ERS SAR. *ESA Earth Observation Quarterly, 52*.

Salisbury, J. W., D'Aria, D. M., & Sabins, F. F., Jr. (1993). Thermal infrared remote sensing of crude oil slicks. *Remote Sensing of Environment, 45,* 225−231.

Stehman, S. V. (1997). Selecting and interpreting measures of thematic classification accuracy. *Remote Sensing of Environment, 62,* 77−89.

Thomas, I. L., Ching, N. P., Benning, V. M., & D'Aguanno, J. A. (1987). A review of multichannel indices of class separability. *International Journal of Remote Sensing, 8,* 331−350.